Electrocatalysis

Deutsche Ausgabe: DOI: 10.1002/ange.201602802
Internationale Ausgabe: DOI: 10.1002/anie.201602802

Selenium-Enriched Nickel Selenide Nanosheets as a Robust Electrocatalyst for Hydrogen Generation

*Fengmei Wang[+], Yuanchang Li[+], Tofik Ahmed Shifa, Kaili Liu, Feng Wang, Zhenxing Wang, Peng Xu, Qisheng Wang, and Jun He**

Abstract: *To address the urgent need for clean and sustainable energy, the rapid development of hydrogen-based technologies has started to revolutionize the use of earth-abundant noble-metal-free catalysts for the hydrogen evolution reaction (HER). Like the active sites of hydrogenases, the cation sites of pyrite-type transition-metal dichalcogenides have been suggested to be active in the HER. Herein, we synthesized electrodes based on a Se-enriched $NiSe_2$ nanosheet array and explored the relationship between the anion sites and the improved hydrogen evolution activity through theoretical and experimental studies. The free energy for atomic hydrogen adsorption is much lower on the Se sites (0.13 eV) than on the Ni sites (0.87 eV). Notably, this electrode benefits from remarkable kinetic properties, with a small overpotential of 117 mV at 10 mA cm^{-2}, a low Tafel slope of 32 mV per decade, and excellent stability. Control experiments showed that the efficient conversion of H^+ into H_2 is due to the presence of an excess of selenium in the $NiSe_2$ nanosheet surface.*

The global community is facing an unprecedented increase in energy demand. Aside from the escalating demand scenario, the cleanest way of harnessing/storing energy is an important aspect to be critically considered.[1] Thus tremendous efforts have been devoted to make use of abundant and convenient energy sources, lessening our reliance on fossil fuels. Electrocatalytic water splitting for the generation of hydrogen gas is an environmentally friendly alternative to meet the global energy demands.[2] Platinum group metals are the benchmark catalysts for electrocatalytic hydrogen evolution.[3] However, their high costs and low abundance have hindered their large-scale practical application. Thus the discovery of inexpensive electrocatalysts that are based on earth-abundant elements has received significant interest.[4] For example, earth-abundant transition-metal dichalcogenides (TMDs) promote water splitting by catalyzing both the hydrogen evolution reaction (HER) and the oxygen evolution reaction (OER).[2,5] Many two-dimensional layered TMDs, such as MoS_2,[6] and WS_2,[7] catalyze the HER in acidic electrolytes. Unfortunately, both density functional theory (DFT) calculations and experimental investigations have confirmed that the superior HER catalytic activity of these materials is derived from the edges rather than the basal planes.[6a,8] Furthermore, their low electrical conductivity reduces the catalytic efficiency.[9] As a result, other inexpensive TMDs, such as various pyrite-structured TMDs (MX_2; M = Fe, Co, or Ni and X = S or Se), that are found in minerals or sedimentary deposits[10] have emerged as earth-abundant electrocatalysts with high catalytic activity towards the HER. Some of them, such as CoS_2,[11] $CoSe_2$,[12] and $NiSe_2$,[13] benefit from their intrinsic metallic properties. $NiSe_2$ is a Pauli paramagnetic metal with a resistivity below $10^{-3}\ \Omega\,cm$.[14] The metallicity of $NiSe_2$ makes it use in energy-conversion applications appealing. It has been utilized as an efficient electrocatalyst as a Pt-free counter electrode of dye-sensitized solar cells[15] and as an energy storage material.[16] Admittedly, its potential utilization as a HER catalyst has also been studied,[13] and $NiSe_2$ catalysts were found to perform remarkably well in the HER in acidic electrolytes and demonstrated impressive stability. Previously, the reduced, coordinated surface cations (Ni^{2+}, Co^{2+}, and Fe^{2+}), bearing certain similarities to the active centers of hydrogenases, have been suggested to be the active sites of these pyrite electrocatalysts.[10a,b] Unfortunately, up to now, no direct evidence has been described to support the hypothesis that these sites are responsible for the high catalytic HER activity of $NiSe_2$ catalysts. This information is prerequisite for further catalyst optimization, and the mechanism responsible for the high HER catalytic activity of $NiSe_2$ also needs to be explored.

Beyond addressing these issues, the design of $NiSe_2$ nanomaterials as catalysts for the HER is of great importance. As a representative surface chemical reaction, the HER process is governed by two crucial factors. First, the active sites should be intrinsically active catalytic sites, which is determined by their chemical composition and the interactions between different components.[17] Second, the active sites should be easily accessible to the HER-relevant species (e.g., H^+, H_2), and the material should thus display good transport properties, which are determined by the specific surface area and the porous structure. For instance, edge-oriented[18] and metallic MoS_2[19] and WS_2[7a,20] are superior HER catalysts. Likewise, it is of great importance to engineer the surface composition and configuration of $NiSe_2$ through controllable synthesis techniques, thereby improving their

[*] F. M. Wang,[+] T. A. Shifa, K. Liu, F. Wang, Prof. Z. Wang, Prof. J. He
CAS Key Laboratory of Nanosystem and Hierarchical Fabrication
National Center for Nanoscience and Technology
Beijing 100190 (China)
E-mail: hej@nanoctr.cn
F. M. Wang,[+] T. A. Shifa, K. Liu, F. Wang
University of Chinese Academy of Sciences
Beijing 100049 (P.R. China)
Prof. Y. Li,[+] P. Xu, Q. Wang
National Center for Nanoscience and Technology
Beijing 100190 (China)
[+] These authors contributed equally to this work.

Supporting information for this article can be found under: http://dx.doi.org/10.1002/anie.201602802.

HER performance. Herein, we prepared textured $NiSe_2$ nanosheet arrays on flexible electrodes through selenization. This electrode demonstrated high HER activity and stability in acidic water, with a remarkably low overpotential of 117 mV at 10 mA cm^{-2} and a Tafel slope of 32 mV per decade. Our experiments and DFT calculations corroborate that the Se sites and the Se–Se bonds of $NiSe_2$ dominate the striking HER activity on the low-index surface. Furthermore, this selenization method leads to an enrichment of the $NiSe_2$ nanosheet arrays with elemental Se, which is indispensable for facilitating charge transfer and hence improving the catalytic activity.

The vapor selenization technique was utilized to convert ultrathin $Ni(OH)_2$ nanosheets (Supporting Information, Figure S1 and Note SI) into $NiSe_2$ nanosheets in a quartz socket tube under argon atmosphere (Figure S2). Different products were obtained at different temperatures. The as-prepared samples were then analyzed by scanning electron microscopy (SEM; Figure S3). As seen in Figure 1a, uniform and vertically textured $NiSe_2$ nanosheets covering the entire carbon fibers (CFs) were obtained at 450 °C ($NiSe_2$-450) in a selenium atmosphere. Energy-dispersive X-ray (EDX) elemental mappings (Figure 1b) of Ni and Se indicate the fairly homogeneous distribution of the constituents across the nanosheet. The morphologies and microstructures of $NiSe_2$ samples prepared at different temperatures were investigated by transmission electron microscopy (TEM) and high-resolution TEM (HRTEM; Figure 1c and Figure S4). The $NiSe_2$-450 nanosheets consist of many loosely bound nanoparticles with sizes of roughly 30 nm (Figure 1c, inset). By contrast, when the reaction temperature is decreased to 400 °C, the obtained nanosheets consist of loosely held nanoparticles ($NiSe_2$-400; Figure S4a). An increase in reaction temperature resulted in the formation of smaller nanoparticles ($NiSe_2$-500; Figure S4b). HRTEM imaging and the corresponding selected-area electron diffraction (SAED) pattern in Figure 1c clearly confirm the high crystallinity of the nanoparticles. The lattice fringes with a spacing of 0.267 nm are in good agreement with the (210) planes of $NiSe_2$.

The crystal structure of the as-prepared $NiSe_2$ nanosheets was determined by X-ray diffraction (XRD). Aside from the peaks that are due to the CFs ("*"), all other peaks in Figure 1d can be indexed to cubic $NiSe_2$ ($a = 5.962$ Å, PDF No. 88-1711). It possesses a pyrite structure in which the Ni atoms are surrounded by an octahedral arrangement of adjacent Se atoms (Figure 1d, inset). No secondary phase or any other impurity phases were detected, confirming the purity of the product. Furthermore, the reaction temperature has no effect on the crystal type (Figure S5a). Confocal micro-Raman spectra obtained by excitation with an unpolarized 532 nm laser (Figure 1e and Figure S5b) show four peaks at 148, 168, 210, and 239 cm^{-1} for all $NiSe_2$ samples. The two weak peaks at low energy correspond to the vibration modes (T_g and E_g) of dumbbell-shaped Se_2 whereas the two strong peaks at higher energy correspond to the stretching modes of Se–Se pairs (A_g and T_g).[21] A small peak centered at around 250 cm^{-1}, which is the resonance peak of amorphous elemental selenium, was observed in the Raman spectra of all as-prepared $NiSe_2$ samples.[22] Furthermore, the EDX spectrum in Figure S6 reveals the presence of excess elemental Se with a Ni/Se ratio close to 1:2.7. To gain further insight into the elemental bonding configuration and surface chemical composition of $NiSe_2$-450, we characterized the sample by X-ray photoelectron spectroscopy (XPS). As shown in Figure 2a, the XPS spectrum of $NiSe_2$-450 in the Se 3d region contains an important feature. Selenium atoms in $NiSe_2$-450 possess two valence states. The peaks at higher binding energies (54.9 eV and 55.7 eV) could be ascribed to the Se $3d_{5/2}$ and Se $3d_{3/2}$ states of elemental Se, suggesting the presence of elemental Se on the surface.[23] This result is consistent with the Raman and EDX analyses. The other two peaks at 54.6 eV (Se $3d_{5/2}$) and 55.2 eV (Se $3d_{3/2}$) are due to the $NiSe_2$ phase.[13] The peak

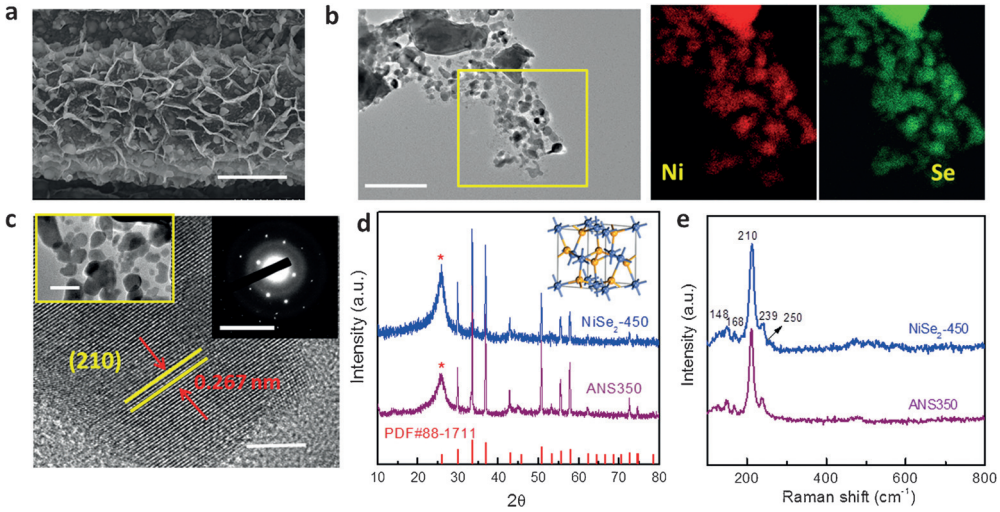

Figure 1. Structural characterization of the $NiSe_2$ nanostructures. a) SEM image of the as-synthesized $NiSe_2$-450 nanosheets on CFs. Scale bar: 5 μm. b) STEM-EDX elemental mapping of the $NiSe_2$-450 nanosheet, showing the homogeneous distribution of Ni and Se. Scale bar: 200 nm. c) HRTEM image of the $NiSe_2$-450 nanosheets. Insets: Corresponding TEM image (left) and SAED pattern (right). Scale bars: 5 nm, 50 nm, and 1 nm^{-1}, respectively. d) XRD patterns of the $NiSe_2$-450 and ANS350 samples compared to that of cubic $NiSe_2$ (PDF No. 88-1711). Inset: Crystal structure of cubic pyrite $NiSe_2$ (Ni cyan, Se yellow). All peaks that are due to the carbon fibers are labeled with "*". e) Raman spectra of the $NiSe_2$-450 and ANS350 nanosheets. The obvious Raman shift at around 250 cm^{-1} indicates the presence of amorphous selenium. ANS350 refers to an as-grown $NiSe_2$-450 sample further annealed at 350 °C under argon atmosphere.

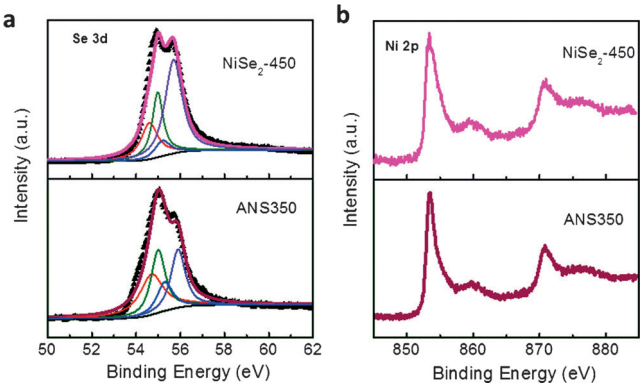

Figure 2. Surface chemical analysis of the different products. a, b) Se 3d and Ni 2p regions of the XPS spectra of the $NiSe_2$-450 and ANS350 nanosheets. In (a), the peaks at 54.9 eV (green curve) and 55.7 eV (violet curve) were ascribed to the Se $3d_{5/2}$ and Se $3d_{3/2}$ of elemental Se species, suggesting the presence of elemental Se on the surface.

assigned to Ni $2p_{3/2}$ was detected at 853.2 eV (Figure 2b and Note SII). These characterizations confirm that a Se-enriched surface is obtained through the selenization reaction in the quartz socket tube. To effectively control the amount of elemental selenium, we annealed the as-grown $NiSe_2$-450 sample at 350 °C ("ANS350"), which is above the melting point of Se and below the temperature of the reaction, under a flow of argon.[24] After the treatment, the morphology of the nanosheets remained unchanged (Figure S7). Figure 1d reveals that the crystal structure of the as-prepared ANS350 is the same as that of the $NiSe_2$-450 sample. However, its peak at about 250 cm^{-1} in the Raman spectrum (Figure 1e) is inconspicuous. The XPS spectrum of ANS350 (Figure 2b) shows an apparent peak at low binding energy in the Se 3d region, indicating a decrease in the amount of elemental Se on the surface. There are only negligible changes in the XPS spectrum in the Ni 2p region (Figure 2b). Furthermore, the Ni/Se ratio determined by XPS analysis was found to be close to 1:1.5 for ANS350 and 1:3.2 for $NiSe_2$-450. The Se content is clearly significantly lower in ANS350. Therefore, the Raman, EDX, and XPS results unequivocally confirm the presence of elemental Se on the surface of the as-grown $NiSe_2$ nanosheet arrays. Encouraged by the terrific performance and stability of selenium-modified Ru catalysts in the oxygen reduction reaction in acidic media,[25] we speculated that the elemental Se on the surface of $NiSe_2$-450 may facilitate hydrogen evolution (see below).

Next, the HER catalytic characteristics of the $NiSe_2$ electrodes were evaluated in N_2-saturated H_2SO_4 electrolyte and compared to those of platinum foil (see the Supporting Information for details). The ohmic potential drop (iR) losses from the solution resistance were corrected (Figure S8). As seen in Figure 3a, the CF substrate has a negligible HER performance with a featureless polarization curve. Notably, the Se-rich $NiSe_2$-450 electrode achieved a current density of 10 mA cm^{-2} at a low overpotential of 117 mV (η_{10}), which is lower than those recently reported for other binary pyrite structures.[13,26] This electrode demonstrates the best HER catalytic performance among all synthesized samples, with η_{10} values of 125 mV and 129 mV for $NiSe_2$-400 and $NiSe_2$-500, respectively (Figure S9). In an attempt to explore these differences between the as-grown $NiSe_2$ based samples, the double-layer capacitances (C_{dl}) were utilized to estimate the effective electrochemically active area of the solid–liquid interface (Note SIII, Figures S10a–c and 11a).[11a] The optimized electrochemically active surface area of $NiSe_2$-450, whose C_{dl} value is 1.7 times than that of $NiSe_2$-500, contributes to the observed superior activity (Table S1). For comparison, a higher overpotential of 152 mV was obtained at the same current density (10 mV cm^{-2}) for the ANS350 electrode in spite of its slightly larger active surface area compared to that of $NiSe_2$-450 (Figure S10d and S11b). Thus, the poorer HER performance of ANS350 can mostly be attributed to the loss of elemental Se from the surface. Figure 3b summarizes the overpotentials of different electrocatalysts at 1 and 10 mA cm^{-2}. Furthermore, the Se-rich $NiSe_2$-450 nanosheets exhibited a smaller onset potential of approximately 71 mV, demonstrating their better catalytic performance compared to ANS350 nanosheets with an onset potential of about 129 mV (Figure S12 and Table S2). These results indicate that all $NiSe_2$ based electrodes are better catalysts than ANS350. Aside from the large surface area, the superior HER activity of $NiSe_2$-450 is believed to arise from the abundant elemental Se on the surface. The corresponding Tafel plots shown in Figure 3c yield slopes of 32 mV dec^{-1} ($NiSe_2$-450) and 31 mV dec^{-1} (ANS350), which are comparable to that of Pt foil (31 mV^{-1}). These small Tafel slopes for all samples (Figure 3d) indicate a two-electron transfer process following a Volmer–Tafel mechanism of bimolecular adsorption and hydrogen evolution occurring on the surface of these catalysts. This mechanism is consistent with that on Pt.[3c] To further corroborate the importance of Se enrichment on $NiSe_2$-450, different ANS samples were prepared through reducing the annealing temperature (280 and 320 °C). Excessive Se could be stripped off from the $NiSe_2$ surface by changing the annealing temperature; thus the amount of surface Se can be controlled without destroying the $NiSe_2$ crystal structure. These ANS280 and ANS320 samples exhibited slightly better catalytic activities for the HER (Figure 3e and Figure S9) than ANS350 in connection to their remnant content of surface Se. Meanwhile, the exchange current density (j_0), the most inherent measure of the HER activity, was carefully determined to assess the quality of the $NiSe_2$ and ANS samples. The j_0 value of 4.7×10^{-3} mA cm^{-2} for the $NiSe_2$-450 electrode surpasses the value of 1.3×10^{-4} mA cm^{-2} for ANS350 as well as the values reported for $NiSe_2$ HER catalysts.[13] In particular, after being normalized by the relative surface area,[11a] the larger normalized exchange current density ($J_{0,normalized}$) of $NiSe_2$-450 compared to that of ANS350 implies the improved intrinsic activity of the Se-enriched $NiSe_2$ material (Table S1). Electrochemical impedance spectroscopy (EIS) was used to provide further insight into the electrode kinetics of the HER process. The Nyquist plots for $NiSe_2$-450 and ANS350 at an overpotential of 0.1 V are shown in Figure 3f. Circuit model fitting analysis of the EIS suggests that both electrodes can be modeled using a modified equivalent circuit consisting of a series resistance (R_s), a constant phase element (CPE), and a charge transfer resistance (R_{ct}). The very small observed R_{ct} value of only

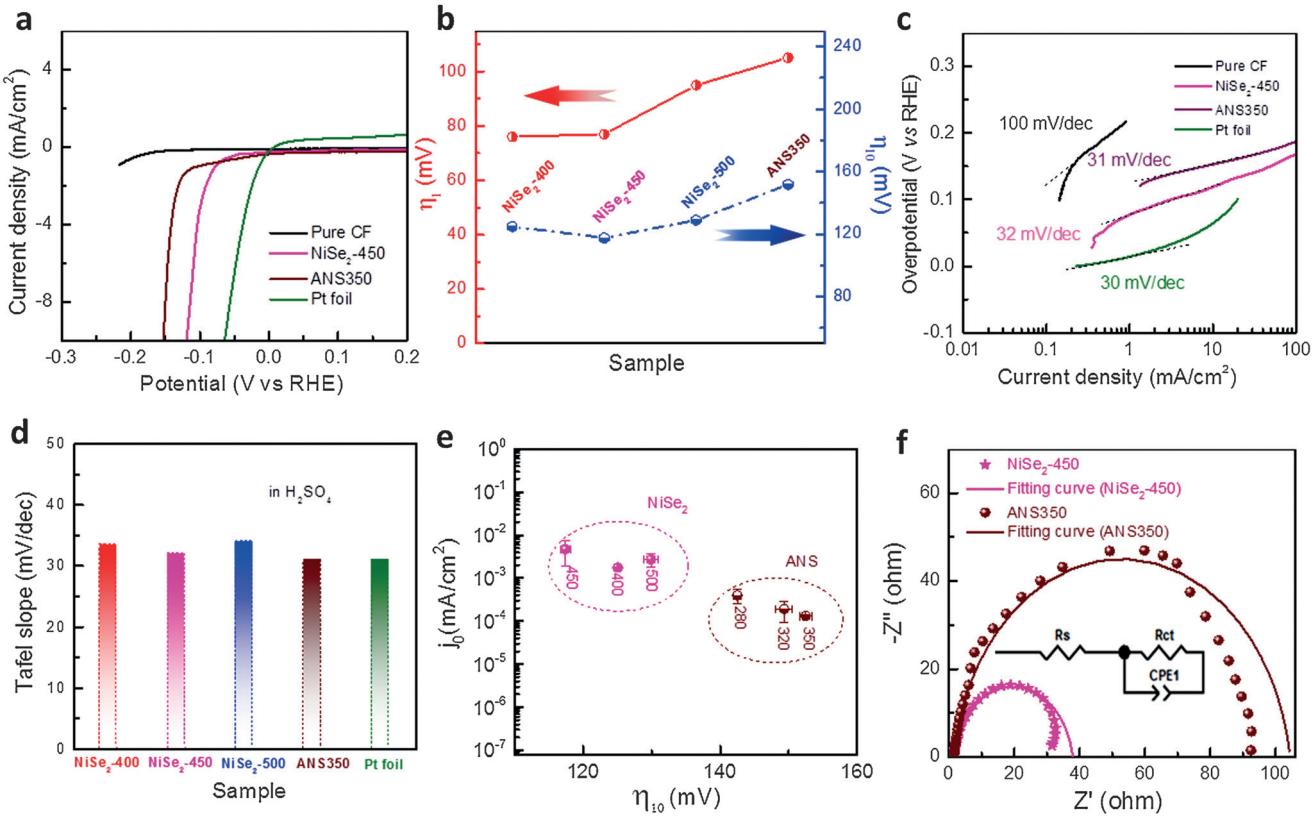

Figure 3. Electrochemical characterization of $NiSe_2$ and ANS nanosheets on carbon fiber electrodes for HER catalysis. a) Polarization curves for HER with different CF electrodes covered by $NiSe_2$-450 and ANS350 nanosheets in H_2SO_4 electrolyte (pH ≈ 0.67) in comparison to a Pt foil and pure CF. Sweep rate: 5 $mV s^{-1}$. b) The variation in overpotential at current densities of 1 and 10 $mA cm^{-2}$ obtained from (a). c) Tafel plot for the various catalysts derived from (a). d) Comparison of the Tafel slopes of the different $NiSe_2$ and ANS350 electrodes and Pt foil. e) Statistical summary of the j_0 values versus the overpotential at 10 $mA cm^{-2}$ for all $NiSe_2$ and ANS electrodes, demonstrating the better HER activity of $NiSe_2$ electrodes compared to that of ANS electrodes. f) Electrochemical impedance spectroscopy (EIS) Nyquist plots for the $NiSe_2$-450 and ANS350 electrodes. The data were fitted using the modified Randles circuits shown in the inset.

32 Ω for $NiSe_2$-450, which is much smaller than that of 103 Ω for ANS350, indicates a fast Faradic process and thus superior HER kinetics. The high j_0 value and the small R_{ct} signal suggest that the elemental Se acts as a promoter, facilitating the charge transfer on the surface to achieve efficient conversion of H^+ into H_2 bubbles. We hypothesize that the interaction and synergy between $NiSe_2$ and Se is vital to sustain the HER activity. The intrinsic properties of the active sites were shown to be improved when elemental Se modifies the $NiSe_2$ surface, and the interface between them is thus proposed to be the efficient active site in this system. Thus, the established functional link potentially endows the surface with much more pronounced activity for the HER.

Given the high electrocatalytic activity of Se-rich $NiSe_2$-450 towards the HER, we further studied its stability to continuously catalyze the generation of H_2. After 1000 and 3000 cyclic voltammetry cycles within 6 hours, a negligible decay was observed at high current density, and massive H_2 bubbles were generated on the surface of the electrode (Figure 4a). The H_2 generation can proceed at a constant current density of −12.5 $mA cm^{-2}$ even over 67 h of continuous operation (Figure 4b,c, see also Movie S1). The time-dependent curve of the $NiSe_2$-450 electrode is of a typical serrate shape (Figure 4b, inset) because of the alternating processes of bubble accumulation and release. During this process, high-purity nitrogen gas was continuously bubbled into the solution to avoid the accumulation of H_2 gas and maintain the N_2 saturation. Remarkably, after the stability measurements, XPS studies in the Se 3d and Ni 2p region revealed no obvious changes in the chemical state (Figure 4d,e), confirming the robustness of the catalyst. A weak peak around 59 eV in the Se 3d region indicated that a small amount of SeO_2 had been formed on the surface by oxidation in air. The morphology and crystal phase of the sample were almost preserved as confirmed by the SEM images in Figure S13 and the XRD pattern in Figure 4f, respectively.

We further carried out first-principles calculations (see the Supporting Information for details) to evaluate the HER activity of $NiSe_2$. We took the (110) surface as an example as both Ni and Se sites can coexist on this surface as shown in Figure 5a. Hydrogen atoms are attached to Se and Ni sites as illustrated in Figure 5b and 5c, respectively. Note that there is more than one kind of Se and Ni site for hydrogen adsorption (see Figure S14). Figure 5d summarizes the calculated free energies (ΔG_{H^*}). The Se and Ni sites have free energies of 0.13 and 0.87 eV, respectively. Therefore, the Se sites are

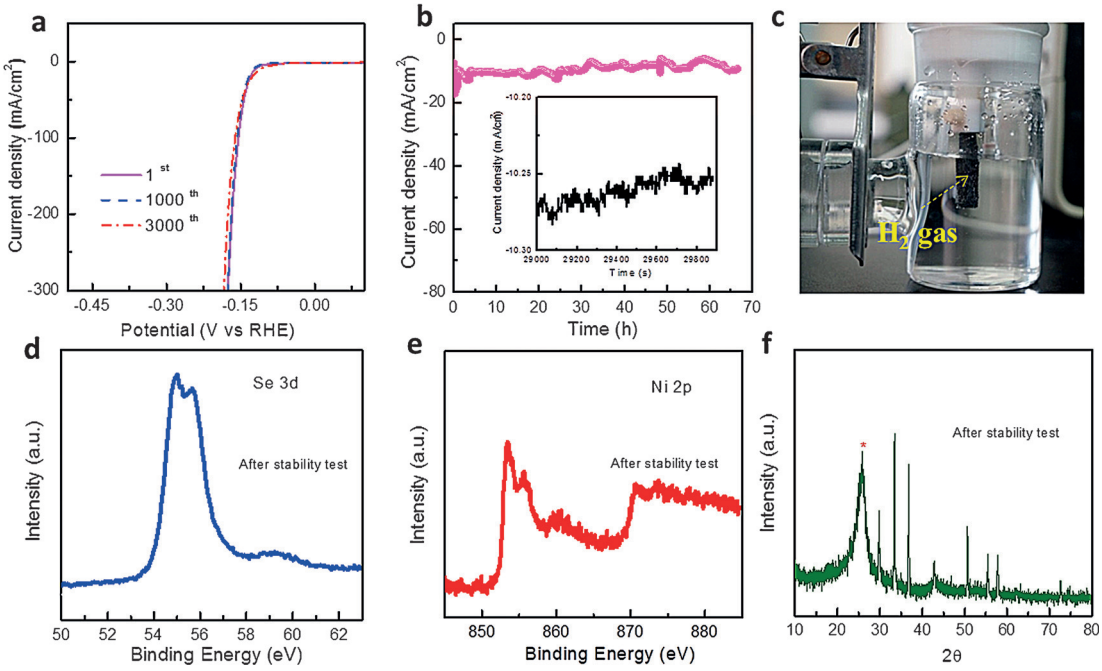

Figure 4. Stability tests for the $NiSe_2$–450 electrode. a) Comparison of the polarization curves after continuous sweeps at 100 $mV s^{-1}$ in acidic (H_2SO_4) media. b) Time dependence of the current density (about -12.5 $mA cm^{-2}$) during electrolysis for 67 h at a fixed overpotential of -150 mV. c) Photograph of the process in (b), showing the formation of H_2 bubbles on the surface. d–f) The Se 3d and Ni 2p regions of the XPS spectrum and the XRD pattern of the $NiSe_2$-450 nanosheets after the stability test, suggesting that no obvious changes had occurred.

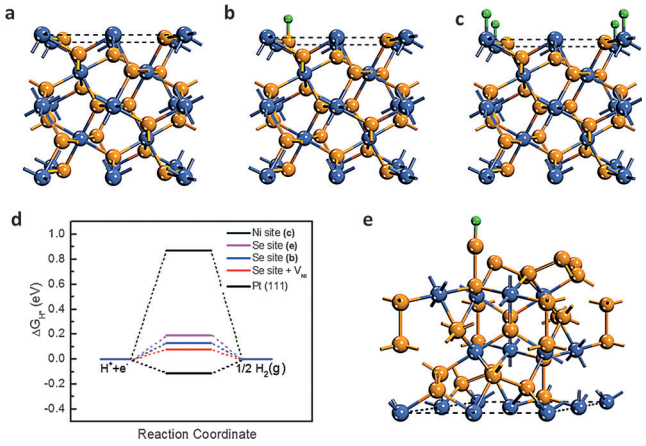

Figure 5. Free-energy diagram from first-principles calculations. a) Slab model of the $NiSe_2$ (110) surface, where both Ni and Se atoms are present in the termination layer. Hydrogen adsorption at b) Se sites and c) Ni sites. d) Free energy (ΔG_{H^*}) diagram for different hydrogen-adsorbed states. e) Hydrogen adsorption at a Se-terminated (111) surface. In (d), the red line corresponds to the configuration with a surface Ni (four-coordinated) atom removed from (b). H green, Ni cyan, Se yellow. The black dashed rhomboids denote the surface unit cells.

responsible for the good catalytic activity of $NiSe_2$, but not the previously assumed Ni sites.[10a,b,12] In our experiment, the Se-enriched $NiSe_2$-450 sample, with a Ni/Se ratio of 1:3.2, exhibited the best performance. To mimic such a Se-rich environment, we removed one Ni atom on the terminated surface and then calculated the free energy for hydrogen adsorption on the same Se site. It was found that the free energy becomes 0.08 eV, approaching zero. On the other hand, a Se-rich environment may arise from the adsorption of excess Se on $NiSe_2$ surface. Figure 5e shows a Se-terminated (111) surface, in which the topmost Se atom only binds to another Se atom underneath. We expect that such a model can partially describe the Se adsorption case. It gives a free energy of 0.19 eV. Note, however, that such a Se atom is unstable for the adsorption of more that one hydrogen atom, even if it has a better free energy of 0.02 eV. All of these results suggest that the Se centers are the active sites for the HER rather than the Ni sites in $NiSe_2$. Whereas excess Se on the surface can considerably improve the overall performance, elemental Se particles would suffer from low stability. Therefore, careful interface engineering is necessary to achieve a good balance between HER activity and stability.

In summary, we have presented selenium-enriched pyrite-type $NiSe_2$ as an efficient high-performance and earth-abundant catalyst for robust electrochemical hydrogen evolution. Aside from the large accessible surface area, the excess selenium on the $NiSe_2$ surface accelerates the changer transfer during the HER process as they optimize the intrinsic catalytic capacity of the $NiSe_2$ nanosheets to a certain extent and act as promoters for H_2 production. In combination with DFT calculations, we showed that the Se sites and the Se–Se bonds of $NiSe_2$ are of critical importance for the striking HER activity and stability.

Acknowledgements

This work was supported by the National Natural Science Foundation of China (21373065 and 61474033), the 973 Program of the Ministry of Science and Technology of China (2012CB934103), the Beijing Natural Science Foundation (2144059), and CAS Key Laboratory of Nanosystem and Hierarchical Fabrication. We gratefully thank the K. C. Wong Education Foundation for support.

Keywords: chalcogenides · electrocatalysis · hydrogen evolution reaction · nickel · selenium

How to cite: *Angew. Chem. Int. Ed.* **2016**, *55*, 6919 – 6924
Angew. Chem. **2016**, *128*, 7033 – 7038

[1] a) J. A. Turner, *Science* **2004**, *305*, 5686; b) M. Chhowalla, H. S. Shin, G. Eda, L.-J. Li, K. P. Loh, H. Zhang, *Nat. Chem.* **2013**, *5*, 263 – 275; c) M. Grätzel, *Nature* **2001**, *414*, 338 – 344; d) Y. Wang, Q. Wang, X. Zhan, F. Wang, M. Safdar, J. He, *Nanoscale* **2013**, *5*, 8326 – 8339.

[2] F. Wang, T. A. Shifa, X. Zhan, Y. Huang, K. Liu, Z. Cheng, C. Jiang, J. He, *Nanoscale* **2015**, *7*, 19764 – 19788.

[3] a) J. Greeley, T. F. Jaramillo, J. Bonde, I. Chorkendorff, J. K. Nørskov, *Nat. Mater.* **2006**, *5*, 909 – 913; b) B. Hinnemann, P. G. Moses, J. Bonde, K. P. Jørgensen, J. H. Nielsen, S. Horch, I. Chorkendorff, J. K. Nørskov, *J. Am. Chem. Soc.* **2005**, *127*, 5308 – 5309; c) B. E. Conway, B. V. Tilak, *Electrochim. Acta* **2002**, *47*, 3571 – 3594; d) Z. Fan, Z. Luo, X. Huang, B. Li, Y. Chen, J. Wang, Y. Hu, H. Zhang, *J. Am. Chem. Soc.* **2016**, *138*, 1414 – 1419.

[4] M. S. Faber, S. Jin, *Energy Environ. Sci.* **2014**, *7*, 3519 – 3542.

[5] a) Q. Lu, Y. Yu, Q. Ma, B. Chen, H. Zhang, *Adv. Mater.* **2016**, *28*, 1917 – 1933; b) J. Miao, F. X. Xiao, H. B. Yang, S. Y. Khoo, J. Chen, Z. Fan, Y.-Y. Hsu, H. M. Chen, H. Zhang, B. Liu, *Sci. Adv.* **2015**, *1*, e1500259; c) J. Chen, X. J. Wu, L. Yin, B. Li, X. Hong, Z. Fan, B. Chen, C. Xue, H. Zhang, *Angew. Chem. Int. Ed.* **2015**, *54*, 1210 – 1214; *Angew. Chem.* **2015**, *127*, 1226 – 1230; d) C. B. Ma, X. Qi, B. Chen, S. Bao, Z. Yin, X. J. Wu, Z. Luo, J. Wei, H. L. Zhang, H. Zhang, *Nanoscale* **2014**, *6*, 5624 – 5629; e) Z. Zeng, C. Tan, X. Huang, S. Bao, H. Zhang, *Energy Environ. Sci.* **2014**, *7*, 797 – 803; f) X. Huang, Z. Zeng, S. Bao, M. Wang, X. Qi, Z. Fan, H. Zhang, *Nat. Commun.* **2013**, *4*, 1444.

[6] a) T. F. Jaramillo, K. P. Jørgensen, J. Bonde, J. H. Nielsen, S. Horch, I. Chorkendorff, *Science* **2007**, *317*, 100 – 102; b) J. V. Lauritsen, J. Kibsgaard, S. Helveg, H. Topsoe, B. S. Clausen, E. Laegsgaard, F. Besenbacher, *Nat. Nanotechnol.* **2007**, *2*, 53 – 58; c) Y. Tan, P. Liu, L. Chen, W. Cong, Y. Ito, J. Han, X. Guo, Z. Tang, T. Fujita, A. Hirata, M. W. Chen, *Adv. Mater.* **2014**, *26*, 8023 – 8028; d) Y. Yan, B. Xia, Z. Xu, X. Wang, *ACS Catal.* **2014**, *4*, 1693 – 1705; e) H. Li, C. Tsai, A. L. Koh, L. Cai, A. W. Contryman, A. H. Fragapane, J. Zhao, H. S. Han, H. C. Manoharan, F. Abild-Pedersen, J. K. Norskov, X. Zheng, *Nat. Mater.* **2016**, *15*, 48 – 53.

[7] a) D. Voiry, H. Yamaguchi, J. Li, R. Silva, D. C. B. Alves, T. Fujita, M. Chen, T. Asefa, V. B. Shenoy, G. Eda, M. Chhowalla, *Nat. Mater.* **2013**, *12*, 850 – 855; b) K. Xu, F. Wang, Z. Wang, X. Zhan, Q. Wang, Z. Cheng, M. Safdar, J. He, *ACS Nano* **2014**, *8*, 8468 – 8476; c) Y. Jung, J. Shen, Y. Liu, J. M. Woods, Y. Sun, J. J. Cha, *Nano Lett.* **2014**, *14*, 6842 – 6849.

[8] A. B. Laursen, S. Kegnaes, S. Dahl, I. Chorkendorff, *Energy Environ. Sci.* **2012**, *5*, 5577 – 5591.

[9] a) X. Zou, Y. Zhang, *Chem. Soc. Rev.* **2015**, *44*, 5148 – 5180; b) Y. Li, H. Wang, L. Xie, Y. Liang, G. Hong, H. Dai, *J. Am. Chem. Soc.* **2011**, *133*, 7296 – 7299.

[10] a) D. Kong, J. J. Cha, H. Wang, H. R. Lee, Y. Cui, *Energy Environ. Sci.* **2013**, *6*, 3553 – 3558; b) M. Cabán-Acevedo, M. L. Stone, J. R. Schmidt, J. G. Thomas, Q. Ding, H.-C. Chang, M.-L. Tsai, J.-H. He, S. Jin, *Nat. Mater.* **2015**, *14*, 1245 – 1251; c) M. S. Faber, M. A. Lukowski, Q. Ding, N. S. Kaiser, S. Jin, *J. Phys. Chem. C* **2014**, *118*, 21347 – 21356; d) X. Wu, B. Yang, Z. Li, L. Lei, X. Zhang, *RSC Adv.* **2015**, *5*, 32976 – 32982; e) H. Zhang, B. Yang, X. Wu, Z. Li, L. Lei, X. Zhang, *ACS Appl. Mater. Interfaces* **2015**, *7*, 1772 – 1779.

[11] a) M. S. Faber, R. Dziedzic, M. A. Lukowski, N. S. Kaiser, Q. Ding, S. Jin, *J. Am. Chem. Soc.* **2014**, *136*, 10053 – 10061; b) S. Peng, L. Li, X. Han, W. Sun, M. Srinivasan, S. G. Mhaisalkar, F. Cheng, Q. Yan, J. Chen, S. Ramakrishna, *Angew. Chem. Int. Ed.* **2014**, *53*, 12594 – 12599; *Angew. Chem.* **2014**, *126*, 12802 – 12807.

[12] D. Kong, H. Wang, Z. Lu, Y. Cui, *J. Am. Chem. Soc.* **2014**, *136*, 4897 – 4900.

[13] J. Liang, Y. Yang, J. Zhang, J. Wu, P. Dong, J. Yuan, G. Zhang, J. Lou, *Nanoscale* **2015**, *7*, 14813 – 14816.

[14] M.-Z. Xue, Z.-W. Fu, *Electrochem. Commun.* **2006**, *8*, 1855 – 1862.

[15] F. Gong, X. Xu, Z. Li, G. Zhou, Z. S. Wang, *Chem. Commun.* **2013**, *49*, 1437 – 1439.

[16] J. A. Reyes-Retana, G. G. Naumis, F. Cervantes-Sodi, *J. Phys. Chem. C* **2014**, *118*, 3295 – 3304.

[17] J. Zhuo, M. Cabán-Acevedo, H. Liang, L. Samad, Q. Ding, Y. Fu, M. Li, S. Jin, *ACS Catal.* **2015**, *5*, 6355 – 6361.

[18] a) M. R. Gao, M. K. Chan, Y. Sun, *Nat. Commun.* **2015**, *6*, 7493; b) D. Kong, H. Wang, J. J. Cha, M. Pasta, K. J. Koski, J. Yao, Y. Cui, *Nano Lett.* **2013**, *13*, 1341 – 1347.

[19] a) D. Voiry, M. Salehi, R. Silva, T. Fujita, M. Chen, T. Asefa, V. B. Shenoy, G. Eda, M. Chhowalla, *Nano Lett.* **2013**, *13*, 6222 – 6227; b) M. A. Lukowski, A. S. Daniel, F. Meng, A. Forticaux, L. Li, S. Jin, *J. Am. Chem. Soc.* **2013**, *135*, 10274 – 10277.

[20] F. Wang, J. Li, F. Wang, T. A. Shifa, Z. Cheng, Z. Wang, K. Xu, X. Zhan, Q. Wang, Y. Huang, C. Jiang, J. He, *Adv. Funct. Mater.* **2015**, *25*, 6077 – 6083.

[21] H. Fan, M. Zhang, X. Zhang, Y. Qian, *J. Cryst. Growth* **2009**, *311*, 4530 – 4534.

[22] a) X. Zhou, P. Gao, S. Sun, D. Bao, Y. Wang, X. Li, T. Wu, Y. Chen, P. Yang, *Chem. Mater.* **2015**, *27*, 6730 – 6736; b) G. W. Tang, Q. Qian, K. L. Peng, X. Wen, G. X. Zhou, M. Sun, X. D. Chen, Z. M. Yang, *AIP Adv.* **2015**, *5*, 027113.

[23] C. Zhang, H. Tao, Y. Dai, X. He, K. Zhang, *Prog. Nat. Sci.: Mater.* **2014**, *24*, 671 – 675.

[24] G. Zehl, G. Schmithals, A. Hoell, S. Haas, C. Hartnig, I. Dorbandt, P. Bogdanoff, S. Fiechter, *Angew. Chem. Int. Ed.* **2007**, *46*, 7311 – 7314; *Angew. Chem.* **2007**, *119*, 7452 – 7455.

[25] a) P. K. Babu, A. Lewera, J. H. Chung, R. Hunger, W. Jaegermann, N. Alonso-Vante, A. Wieckowski, E. Oldfield, *J. Am. Chem. Soc.* **2007**, *129*, 15140 – 15141; b) D. Cao, A. Wieckowski, J. Inukai, N. Alonso-Vante, *J. Electrochem. Soc.* **2006**, *153*, A869.

[26] H. Liang, L. Li, F. Meng, L. Dang, J. Zhuo, A. Forticaux, Z. Wang, S. Jin, *Chem. Mater.* **2015**, *27*, 5702 – 5711.

Received: March 20, 2016
Published online: April 25, 2016

